Co-flow injection for serial crystallography at X-ray free-electron lasers

Diandra Doppler,[a,b]‡ Mohammad T. Rabbani,[a,b]‡ Romain Letrun,[c] Jorvani Cruz Villarreal,[a,b] Dai Hyun Kim,[a,b] Sahir Gandhi,[a,b] Ana Egatz-Gomez,[a,b] Mukul Sonker,[a,b] Joe Chen,[d] Faisal H. M. Koua,[e] Jayhow Yang,[b] Mohamed Youssef,[e] Victoria Mazalova,[e] Saša Bajt,[f,g] Megan L. Shelby,[h] Matt A. Coleman,[h] Max O. Wiedorn,[e,f,i] Juraj Knoska,[e] Silvan Schön,[e] Tokushi Sato,[c] Mark S. Hunter,[j] Ahmad Hosseinizadeh,[k] Christopher Kuptiz,[j] Reza Nazari,[b,d] Roberto C. Alvarez,[b,d] Konstantinos Karpos,[b,d] Sahba Zaare,[b,d] Zachary Dobson,[a,b] Erin Discianno,[b] Shangji Zhang,[a,b] James D. Zook,[a,b] Johan Bielecki,[c] Raphael de Wijn,[c] Adam R. Round,[c,l] Patrik Vagovic,[c,e] Marco Kloos,[c] Mohammad Vakili,[c] Gihan K. Ketawala,[a,b] Natasha E. Stander,[a,b] Tien L. Olson,[a,b] Katherine Morin,[b] Jyotirmory Mondal,[m] Jonathan Nguyen,[a,b] José Domingo Meza-Aguilar,[b,c] Gerdenis Kodis,[a,b,d] Sara Vaiana,[d] Jose M. Martin-Garcia,[b,n] Valerio Mariani,[e] Peter Schwander,[k] Marius Schmidt,[k] Marc Messerschmidt,[a,b] Abbas Ourmazd,[k] Nadia Zatsepin,[b,d,o] Uwe Weierstall,[b,d] Barry D. Bruce,[m] Adrian P. Mancuso,[c,o] Thomas Grant,[p] Anton Barty,[e,g,q] Henry N. Chapman,[e,f,i] Matthias Frank,[h] Raimund Fromme,[a,b] John C. H. Spence,[b,d] Sabine Botha,[b,d] Petra Fromme,[a,b] Richard A. Kirian[b,d] and Alexandra Ros[a,b]*

Received 14 May 2021
Accepted 22 October 2021

Edited by S. Boutet, SLAC National Accelerator Laboratory, Menlo Park, USA

‡ These authors contributed equally.

Keywords: microfluidic devices; serial crystallography; 3D printing; X-ray free-electron lasers; XFELs; viscous media; sample consumption.

Supporting information: this article has supporting information at journals.iucr.org/j

[a]School of Molecular Sciences, Arizona State University, Tempe, Arizona, USA, [b]Center for Applied Structural Discovery, Biodesign Institute, Arizona State University, Tempe, Arizona, USA, [c]European XFEL, Schenefeld, Germany, [d]Department of Physics, Arizona State University, Tempe, Arizona, USA, [e]Center for Free-Electron Laser Science, Deutsches Elektronen-Synchrotron (DESY), Hamburg, Germany, [f]Hamburg Center for Ultrafast Imaging, Hamburg, Germany, [g]Deutsches Elektronen-Synchrotron (DESY), Hamburg, Germany, [h]Lawrence Livermore National Laboratory (LLNL), Livermore, California, USA, [i]Department of Physics, Universität Hamburg, Hamburg, Germany, [j]Linac Coherent Light Source, SLAC National Accelerator Laboratory, Menlo Park, California, USA, [k]Department of Physics, University of Wisconsin-Milwaukee, Milwaukee, Wisconsin, USA, [l]School of Chemical and Physical Sciences, Keele University, Staffordshire, UK, [m]Department of Biochemistry and Cellular and Molecular Biology, University of Tennessee, Knoxville, Tennessee, USA, [n]Department of Crystallography and Structural Biology, Institute of Physical Chemistry 'Rocasolano', CSIC, Madrid, Spain, [o]Department of Chemistry and Physics, La Trobe Institute for Molecular Science, La Trobe University, Melbourne, Australia, [p]Department of Structural Biology, Jacobs School of Medicine and Biomedical Sciences, SUNY University at Buffalo, Buffalo, New York, USA, and [q]Center for Data and Computing in Natural Science CDCS, Deutsches Elektronen-Synchrotron DESY, Hamburg, Germany. *Correspondence e-mail: alexandra.ros@asu.edu

Serial femtosecond crystallography (SFX) is a powerful technique that exploits X-ray free-electron lasers to determine the structure of macromolecules at room temperature. Despite the impressive exposition of structural details with this novel crystallographic approach, the methods currently available to introduce crystals into the path of the X-ray beam sometimes exhibit serious drawbacks. Samples requiring liquid injection of crystal slurries consume large quantities of crystals (at times up to a gram of protein per data set), may not be compatible with vacuum configurations on beamlines or provide a high background due to additional sheathing liquids present during the injection. Proposed and characterized here is the use of an immiscible inert oil phase to supplement the flow of sample in a hybrid microfluidic 3D-printed co-flow device. Co-flow generation is reported with sample and oil phases flowing in parallel, resulting in stable injection conditions for two different resin materials experimentally. A numerical model is presented that adequately predicts these flow-rate conditions. The co-flow generating devices reduce crystal clogging effects, have the potential to conserve protein crystal samples up to 95% and will allow degradation-free light-induced time-resolved SFX.

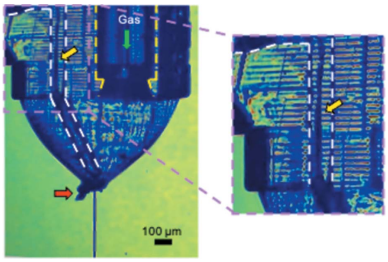

1. Introduction

Serial femtosecond crystallography (SFX) with X-ray free-electron lasers (XFELs) has shown impressive advances in the field of macromolecular structure determination in the past

decade (Martin-Garcia *et al.*, 2016; Chapman *et al.*, 2011; Boutet *et al.*, 2012; Orville, 2020). Examples include revealing structural details of membrane proteins with unprecedented resolution, such as G-protein coupled receptors (Zhang *et al.*, 2015; Kang *et al.*, 2015; Stauch & Cherezov, 2018; Gusach *et al.*, 2020) or photosystems (Kupitz *et al.*, 2014; Gisriel *et al.*, 2019). The recent demonstration of time-resolved (TR) imaging of enzyme catalysis under near-physiological conditions (Stagno *et al.*, 2016; Olmos *et al.*, 2018; Calvey *et al.*, 2016; Pandey *et al.*, 2021), made possible by XFEL crystallography using mixing injectors, further provides a tantalizing glimpse of the dawn of the new field of structural enzymology and its likely impact. This relates to all aspects of life controlled by enzymes and will improve our knowledge for the design of inhibitors to common diseases threatening our health.

Pump–probe TR-SFX with XFELs involves laser pulses triggering a reaction mechanism in light-activated proteins shortly before they are probed by an XFEL beam. This allows time resolution in the range of femtoseconds to microseconds (Neutze *et al.*, 2000; Chapman *et al.*, 2011). However, most biologically relevant processes, such as enzymatic reactions, are not light induced and instead require rapid mixing of the protein crystals with a ligand (*e.g.* a substrate or an antibiotic). Methods facilitating these mix-and-inject experiments are limited by the diffusion of the ligand into the crystals and this typically leads to time scales of the order of milliseconds to seconds, such as demonstrated with BlaC (Olmos *et al.*, 2018; Kupitz *et al.*, 2017), cytochrome c oxidase (Ishigami *et al.*, 2018) and the riboswitch (Stagno *et al.*, 2016).

Sample wastage remains a critical issue for SFX and TR-SFX studies with XFELs (Martin-Garcia *et al.*, 2016; Conrad *et al.*, 2015). Protein crystals are cumbersome to obtain in suspensions of adequate concentration in a sufficiently large volume (>10 ml with hundreds of milligrams of protein) for full data sets. Current XFELs operate at pulse frequencies up to 120 Hz at the LCLS (USA), 60 Hz at SACLA (Japan), 30 Hz at PAL-XFEL (South Korea), 100 Hz at SwissFEL (Switzerland) or megahertz pulse trains repeating at 10 Hz frequency at the EuXFEL (Germany). Thus, for all XFEL instruments, the vast majority of the sample is wasted if sample injection is carried out with any continuous liquid injection technique, such as delivery with a gas dynamic virtual nozzle (GDVN) (DePonte *et al.*, 2008). While this method is robust and has demonstrated great success in the past, it has several key limitations: (i) high flow rates in the tens of microlitres per minute are typically required, and (ii) clogging issues arise very often due to viscous samples, adsorption of crystals to the capillary and tubing during delivery, or agglomeration of larger protein crystals within the nozzles and delivery lines.

Several approaches to reduce sample consumption have been proposed. Viscous jet injectors slowly extruding crystals suspended in a viscous medium, such as lipidic cubic phase or agarose, have been successfully used to deliver samples into the path of the XFEL (Conrad *et al.*, 2015; Weierstall *et al.*, 2014). However, many proteins resist crystallization in viscous media, and the large diameter of the extrusion increases background scatter. Furthermore, these slowly focusing jets are not compatible with the higher-repetition-rate facilities in operation (Grünbein *et al.*, 2018) or under construction (LCLS-II, Menlo Park, California, USA).

Double flow-focusing injectors have been successful at injecting higher-viscosity samples at lower sample flow rates, but the samples may be significantly diluted by the sheath liquid required to achieve high enough flow rates to create a stable jet for data collection (Oberthuer *et al.*, 2017). Drop-on-demand systems have also been developed to synchronize the liquid droplets with the XFEL frequency (Mafuné *et al.*, 2016). Alternatively, pulsing the liquid jet of the GDVN by switching the liquid flow on and off has been proposed, but it produces large droplets and does not function *in vacuo* (James, 2015).

Acoustic injection of protein crystal suspensions can expose a high percentage of the crystals injected and exhibits a high hit rate, though it also suffers from a large background and requires large microcrystals (Roessler *et al.*, 2016). Fixed-target methods that raster an array of immobilized crystals with respect to the XFEL beam have been shown to give a vast reduction in sample consumption and improve hit rates (Hunter *et al.*, 2014). However, problems with preferential orientation of the crystal may prevent full sampling of reciprocal space, limitations arise with high-repetition XFELs and time-consuming array changing is often problematic with short beamtime allocations. Similar issues also apply for the recently developed methods that position droplets of a mixing reagent in a timed manner on fixed targets for TR studies (Mehrabi *et al.*, 2019). Furthermore, an approach combining acoustic droplet generation with a conveyor belt delivery has been shown to be suitable for SFX, but is limited by slow reaction time points for TR-SFX delivery in aqueous solutions (Fuller *et al.*, 2017). As for low-flow-rate viscous jet injectors, issues arise for the microfluidic electrokinetic sample holder (MESH) (Sierra *et al.*, 2012) and its updated version, the concentric MESH injector (coMESH) (Sierra *et al.*, 2016), for short millisecond time points as desired in mix-and-inject experiments and due to multiple crystal hits.

We have recently reported a new approach that encapsulates protein crystals in small droplets of mother liquor in an immiscible phase coupled with GDVN injection (Echelmeier *et al.*, 2019, 2020). The device has been successfully used at the LCLS (Echelmeier *et al.*, 2019), where diffraction from photosystem I was recorded, and more recently at the EuXFEL to determine the structure of the enzyme KDO8PS to 2.8 Å resolution at room temperature (Echelmeier *et al.*, 2020). This method has additional potential to synchronize the arrival of the droplet with the XFEL beam and further minimize sample loss, as demonstrated by the electrical triggering of the droplet release (Kim *et al.*, 2019). To synchronize the droplet generation with the XFEL, a feedback mechanism is required, which is linked to optical detection of the generated droplets. An advantage of this droplet approach to reduce sample waste lies in the small footprint of all necessary components and the fabrication of all elements through 3D-printing technology (Echelmeier *et al.*, 2019, 2020).

Apart from sample consumption issues, liquid jet injection for SFX with XFEL experiments also suffers from issues with

very high viscosity samples. Many proteins, including complex membrane proteins, require crystallization conditions in very high viscosity polyethylene glycol (PEG) solutions which often need to be maintained for injection to ensure crystal quality (Durbin & Feher, 2017; Middaugh *et al.*, 1979; Atha & Ingham, 1981; Conrad *et al.*, 2015; Pandey *et al.*, 2020). Overcoming this limitation could be a major breakthrough to allow more elaborate SFX studies of a larger variety of biologically important proteins.

Our development of the above-mentioned injection scheme based on interleaved immiscible phases, together with the issues arising for high-viscosity injection media, led us to the alternative scheme that we present here. During the characterization of droplet generation in our devices, we found regimes in which the sample and oil phases flowed in parallel towards the GDVN and then formed exceptionally long and stable liquid jets which are important for nozzle lifetime. This 'co-flow' phenomenon was characterized in this work both experimentally and with a theoretical model at various flow rates for the aqueous (Q_a) and oil (Q_o) phases. We further characterized two different materials for the 3D-printed co-flow generators, coupled in a hybrid fashion to a GDVN in one device. We also demonstrate the application of this injection method at the EuXFEL for a viscous sample of photosystem II (PSII) crystals embedded in mother liquor and the compatibility of the employed 3D-printed devices with light-induced TR-SFX.

2. Materials and methods

2.1. Materials

Pentaerythritol triacrylate (PETA), phenylbis(2,4,6-trimethylbenzoyl)phosphine oxide (BAPO), 2-morpholinoethanesulfonic acid (MES), sodium chloride (NaCl), calcium dichloride ($CaCl_2$), magnesium sulfate ($MgSO_4$), polyethylene glycol (PEG, MW 1450), polyethylene glycol methyl ether (MW 5000), perfluorodecalin (PFD) and 1*H*,1*H*,2*H*,2*H*-perfluoro-1-octanol (perfluorooctanol, PFO) were purchased from Sigma–Aldrich, USA. The detergents *n*-dodecyl *β*-maltoside and *n*-heptyl-*β*-D-thioglucopyranoside were purchased in crystallization grade from Glycon Biochemicals GmbH (Luckenwalde, Germany). SU-8 developer was obtained from Microchem, USA. The photoresist IP-S was purchased from Nanoscribe GmbH, Germany. Deionized water (18 MΩ) was supplied from an LA755 Elga purification system (Elga LabWater, USA), and propan-2-ol (isopropyl alcohol, IPA) and ethanol were obtained from VWR Analytical (USA) and Decon Labs (USA), respectively. Fused silica capillaries [360 µm outer diameter (OD), 100 µm inner diameter (ID)] were purchased from Molex, USA. Hardman extra-fast-setting epoxy was purchased from All-Spec, USA.

2.2. Co-flow device design and fabrication

Hybrid devices containing a co-flow junction prior to a GDVN (Fig. 1) were designed and fabricated as described

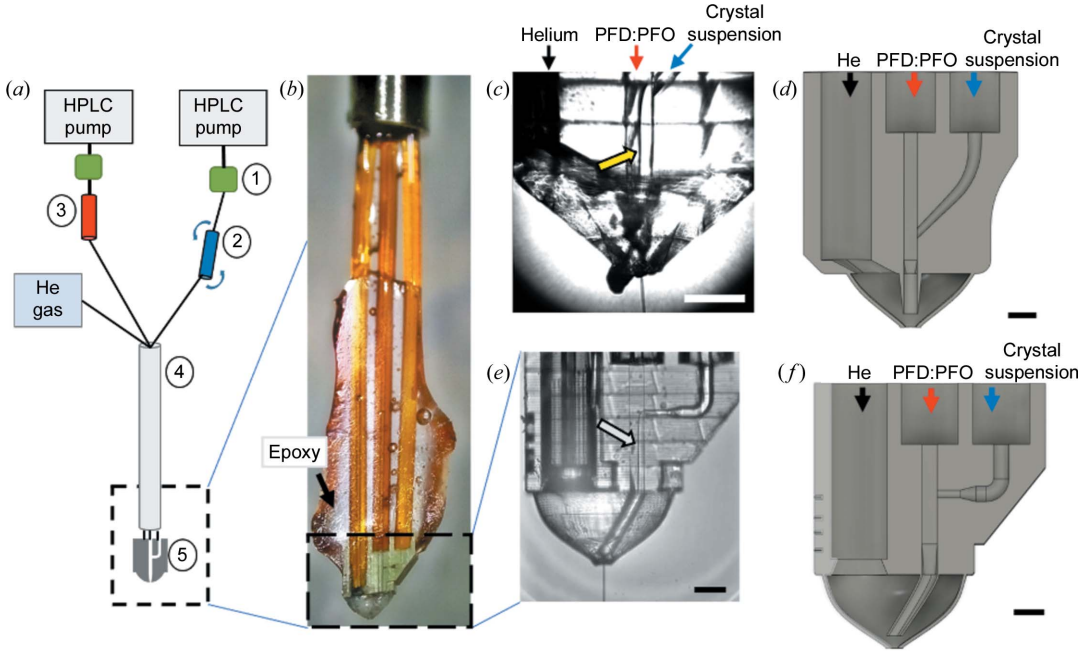

Figure 1
(*a*) The experimental setup of the co-flow generator at the EuXFEL (not to scale). (1) Flow-rate sensors, (2) crystal suspension reservoir mounted in the rotating anti-settler device, (3) oil reservoir, (4) nozzle rod and (5) hybrid device (3D-printed device with integrated co-flow generator and GDVN) mounted on the end of the nozzle rod. Black lines indicate capillary tubing or fused silica capillaries for fluid and gas transport. (*b*) The assembled hybrid device mounted in the nozzle rod. The co-flow/nozzle hybrid is located at the very end of the one gas and two fluidic lines connected to the fused silica capillaries through epoxy. (*c*) An image of the assembled Y-junction device. Co-flow is generated as indicated by the interface between the two phases (see yellow arrow). (*d*) A schematic drawing of the Y-junction device for co-flow formation designed in *Fusion 360*. (*e*) An image of the T-junction hybrid device, showing the oil–sample co-flow running (marked with a white arrow) and the jet leaving the nozzle. (*f*) A schematic drawing of the T-junction device for co-flow formation designed in *Fusion 360*. The scale bars represent 200 µm in panels (*c*)–(*f*).

previously (Echelmeier *et al.*, 2019). Briefly, devices were drawn in *Fusion 360* (AutoDesk, USA) and then 3D-printed with a Photonic Professional GT 3D printer (Nanoscribe GmbH, Germany) using either IP-S photoresist (Nanoscribe GmbH, Germany) or PETA with BAPO (1.2% *w*/*w* BAPO), termed PETA-B. Printing was accomplished in solid mode using dip-in laser lithography (Bückmann *et al.*, 2012) with two-photon polymerization. Once printed, devices were developed in SU-8 developer, or ethanol for PETA-B resin, and rinsed in IPA. Fused silica capillaries were inserted and fixed into the device inlets using epoxy. Their length depended on the experimental setup. At the EuXFEL, 2 m of capillary was attached to each inlet to traverse the length of the nozzle rod, and during preliminary testing in the home laboratory 60 cm of the capillary was used per inlet. The hybrid devices comprised a T-junction or a Y-junction for co-flow formation. The Y-junction is formed by an intersection of a rectangular channel section (100 ×100 µm) and a 75 µm diameter cylindrical channel at a 45° angle. The T-junction is, likewise, formed by a rectangular channel (75 ×100 µm) and a 75 µm diameter cylindrical channel at a 90° angle. These junctions can be seen in the computer-aided designs in Figs. 1(*d*) and 1(*f*). Two iterations of these devices were used for preliminary experiments and injection at the EuXFEL SPB/SFX instrument (Mancuso *et al.*, 2019). Devices containing only capillary inlets and junctions were used for preliminary experiments; experiments performed at the EuXFEL used junctions coupled to GDVNs (Nazari *et al.*, 2020).

2.3. Fluidic operation and setup

High-performance liquid chromatography (HPLC) pumps (LC20AD, Shimadzu Co., Japan) were connected to a custom or commercial stainless steel reservoir containing a plunger through which either crystal suspensions or the oil phase were dispensed (Oberthuer *et al.*, 2017; Wang *et al.*, 2014). Liquid-flow sensors SLI-0430 (Sensirion, Switzerland, accuracy of 5% of measured value, based on the flow rates used in this study up to 1.25 µl min^{-1}) and SLG-0075 (Sensirion, Switzerland, accuracy of 20% of measured flow velocity, based on the flow rates used in this study up to 3.8 µl min^{-1}) were used to monitor the flow rates before the reservoirs. Poly ethyl ether ketone tubing (Zeus, USA, 250 µm ID and 1/16 inch OD) with fittings and ferrules from IDEX Health & Science LLC (USA) was used to connect the HPLC pumps to the sensors and reservoirs. Fused silica capillaries were used to connect the reservoirs to the co-flow devices. During preliminary testing at the ASU laboratory, the device was mounted onto an Olympus IX71 microscope equipped with a Photron Fastcam Mini AX (Photron, USA). Helium gas pressures in the range of 150–600 psi (1 psi $\simeq$ 6893 Pa) were used to operate the GDVNs and controlled manually via a gas regulator. For any flow-rate condition, the system was allowed to equilibrate for 5–10 min until the liquid pressures had stabilized. A schematic diagram of the experimental setup is provided in Fig. 1(*a*). The images obtained from microscopic observation of the co-flow generation were analysed by measuring the width of the aqueous flow using *ImageJ* (Abramoff *et al.*, 2004). The co-flow thickness was assessed at 150 µm from the junction as the width of the aqueous stream in replicates of three.

During experiments at the EuXFEL, the device was mounted in the nozzle rod and inserted through a load–lock system into the vacuum chamber at 1 mPa with the nozzle running (Mancuso *et al.*, 2019; Schulz *et al.*, 2019). Additionally, the reservoir containing the PSII crystals was mounted on a rotating anti-settling device (Lomb *et al.*, 2012) and a GP1 electronic pressure regulator (Equilibar, USA) was used to regulate the helium gas applied to the gas dynamic virtual nozzle. For imaging during the experiments, a Zyla 5.5 sCMOS (Andor, Northern Ireland) equipped with a Mitutoyo MY10X-80310× objective (Thorlabs, USA) was used, and the EuXFEL femtosecond pump–probe laser (800 nm) was employed as the illumination source (Palmer *et al.*, 2019).

2.4. Jet speed characterization

The jet produced by the hybrid co-flow device was illuminated with a double-pulsed fibre-coupled 633 nm 100 ns laser, as previously described (Nazari *et al.*, 2020). A Fastcam SA5 (Photron, USA) camera equipped with a Mitutoyo MY10X-80310× objective (Thorlabs, USA) and a 12× UltraZoom magnifying lens (Navitar, USA) was used to acquire the video needed for the speed analysis. When analysing the acquired video, the translation of the droplets created downstream of the jet where it breaks up is compared with the speed of acquisition. The speed of the jet can be deduced via particle-tracking velocimetry analysis procedures described previously (Adrian, 1991).

2.5. Photoresist laser testing

The 3D-printed structures made of the different photoresists were irradiated using a 532 nm Continuum Surelite Nd:YAG laser (Amplitude Technologies, France). The laser power used ranged from 50 to 360 mJ cm^{-2} at 10 Hz (pulse duration of 5 ns) with a circular (Gaussian profile) laser beam of 1 mm diameter for 10–15 min. The structure was then visually inspected and imaged under a stereomicroscope for damage.

2.6. Crystal sample preparation

The PSII samples were crystallized as described previously (Koua *et al.*, 2013) in the XBI laboratories of the EuXFEL facility (Han *et al.*, 2021). In brief, for homogenous micro-crystal preparations, a detergent exchange from *n*-dodecyl *β*-maltoside to *n*-heptyl-*β*-D-thioglucopyranoside was conducted by precipitation of the PSII with PEG 1450 at a final concentration of 12%(*w*/*v*). The supernatant was discarded and the pellet resuspended in a buffer containing final concentrations of 20 m*M* MES pH 6.0, 20 m*M* NaCl, 5 m*M* $CaCl_2$ and 0.85%(*w*/*v*) *n*-heptyl-*β*-D-thioglucopyranoside. Crystallization was accomplished using 6–7% PEG 1450 as the precipitant at a chlorophyll concentration of 2–4 m*M*. The crystal growth was stopped by adding 2–3%(*w*/*v*) PEG 1450. Microcrystals grew within 1–2 h at 293 K to a range of

10–30 µm. The microcrystals were dehydrated by exchanging the mother liquor with stepwise increasing concentrations of a dehydration buffer to reach final concentrations of 20 m*M* MES pH 6.0, 20 m*M* NaCl, 5 m*M* $CaCl_2$, 22% dimethyl sulfoxide (DMSO), 9%(*w*/*v*) PEG 5000 and 9%(*w*/*v*) PEG 1450. All crystallization steps were performed under dim green light. The microcrystals were loaded in 3 ml aliquots into reservoirs for the injection.

2.7. Diffraction experiments

XFEL experiments were conducted on the SPB/SFX instrument at the EuXFEL (Schenefeld, Germany) (Mancuso *et al.*, 2019; Decking *et al.*, 2020) during beamtime P2326 (September 2019). The pulse structure of the XFEL was composed of 10 Hz bunch trains, with 125 pulses at 564 kHz per bunch train. The pulse duration as estimated from the electron bunch length was 50 fs with a photon energy of 9.31 keV. The beam was focused with Kirkpatrick–Baez mirrors to a beam diameter of about 2.8 × 4.2 µm (Bean *et al.*, 2016). The average pulse energy was ∼600 µJ. Diffraction data were collected using the AGIPD 1 Mpixel detector (Allahgholi *et al.*, 2019; Boukhelef *et al.*, 2013).

2.8. Numerical modelling

Numerical modelling was carried out with the finite-element software *COMSOL Multiphysics* (version 5.4a, COMSOL, Stockholm, Sweden) using the laminar two-phase flow and level set interface in the *Microfluidics* module. The laminar two-phase flow interface considers the Stokes equation in the steady state (Finlayson, 2006),

$$0 = -\nabla p + \mu \nabla^2 \mathbf{u}, \tag{1}$$

where p is the pressure, $\mathbf{u}$ is the velocity vector and μ is the dynamic viscosity. The density is assumed to be constant, representing an incompressible Newtonian fluid ($\nabla \cdot \mathbf{u} = 0$). The fluid velocity is specified at the inlet, and at the outlet the pressure is set as zero.

The level set method (LSM) applies a level set function $\phi(\mathbf{x}, t)$ to the space occupied by the interface, where $\mathbf{x}$ is the coordinate of a location within that space at a specific time t (Bashir *et al.*, 2011). In *COMSOL Multiphysics*, ϕ is a step function which is zero in one domain and one in the other. The function is initialized at time t_0 and then a numerical scheme defines the value of $\phi(\mathbf{x}, t)$ over time. Thus, the propagation of the interface can be traced in time. The fluid interface uses the following equation:

$$\frac{\partial \phi}{\partial t} + \mathbf{u} \cdot \nabla \phi = \gamma \nabla \cdot \left[\varepsilon \nabla \phi - \phi(1 - \phi) \frac{\nabla \phi}{|\nabla \phi|} \right], \tag{2}$$

where γ is the reinitialization parameter and ε is the thickness of the interface. The terms on the right-hand side of equation (2) are necessary for numerical stability, while the terms on the left-hand side define the interface's correct motion. The thickness of the interface ε was adjusted to the largest value of the mesh size. The reinitialization parameter γ was adjusted to the maximum magnitude of the velocity field. Equation (1) was solved to obtain $\mathbf{u}$, which was then used in equation (2) (Deshpande & Zimmerman, 2006).

On the basis of this LSM method, the numerical simulation of the flow behaviour between two immiscible fluids, oil and aqueous buffer, was investigated in the T- and Y-junctions with a 2D (see example images in Fig. S1 in the supporting information) and a 3D model to display the curved interface between the immiscible phases (see example images in Fig. S2). Parameters (Tables S1 and S2) and further details are listed in the supporting information.

3. Results and discussion

Delivering samples in parallel co-flowing streams within a continuous sample-delivery device has the potential to reduce the amount of sample required for SFX experiments. A lubricant oil phase achieves an additional advantage by reducing clogging effects, since the aqueous sample experiences fewer interactions with the capillary walls, and it also facilitates the delivery of crystals in higher-viscosity buffer media. High-viscosity buffers are often encountered in protein crystallization, most frequently in membrane proteins such as PSII (Gisriel *et al.*, 2019; Nazari *et al.*, 2020) or in the case of photoactive yellow protein (Ananyev *et al.*, 2019; Gisriel *et al.*, 2019; Tenboer *et al.*, 2014). Here, we characterized a 3D-printed injection system that allows for co-flow to be generated and subsequently to deliver the sample through a coupled GDVN to the XFEL beam. The associated fluidic line schematic for sample delivery is shown in Fig. 1(*a*), and a photograph of a co-flow nozzle with capillaries attached to deliver liquids and gas is shown in Fig. 1(*b*). The co-flow generator exhibits an oil-phase inlet and an aqueous-phase inlet (for sample), meeting at a Y- or T-shaped intersection as shown in Figs. 1(*c*)–1(*d*) and 1(*e*)–1(*f*), respectively. The two liquids filling the reservoirs are pressurized through HPLC pumps and delivered through fused silica capillaries to the co-flow generator. The oil phase, a 10:1 mixture of PFD and PFO, was chosen because of its immiscibility with PEG-based and DMSO-containing aqueous buffers, as well as its chemical inertness with the protein crystals in the aqueous phase (Echelmeier *et al.*, 2019). The aqueous and oil phases meet at the intersection in the 3D-printed device, where interfacial and shear forces cause them to flow immiscibly in parallel streams. Figs. 1(*c*) and 1(*d*) show, respectively, a microscopic image of the assembled 3D-printed device generating a sample jet and a schematic of the hybrid device with a Y-intersection coupled to a 3D-printed GDVN injector, as recently described by Nazari *et al.* (2020). Figs. 1(*e*) and 1(*f*) show microscopic images of the fabricated 3D-printed device with the T-intersection. The co-flow in each of the two designs is generated shortly after the intersection of the two immiscible fluids and can be observed as a boundary in both Figs. 1(*c*) and 1(*e*).

The establishment of co-flow in these devices was investigated by varying the oil flow (Q_o) and the aqueous flow (Q_a) rates while maintaining a total flow rate Q_{tot} of 20 µl min^{-1}. These conditions were chosen because a total flow rate of

20 µl min^{-1} generated a fast enough jet for the X-ray repetition rate of 564 kHz used during the experiment (see more detail below on jet velocities) and since we found stable co-flow generation at sample flow rates below 10 µl min^{-1}. We explored two different types of resin for 3D-printing the high-resolution co-flow injectors. Figs. 2(*a*) and 2(*b*), respectively, show microscopy images of the T-junction and Y-junction geometries printed with IP-S photoresist. We further investigated two different configurations for generating co-flow with the sample and oil phases. In mode 1, the aqueous sample is delivered from the side channel (*i.e.* the channel connecting to the straight channel), and in mode 2, the aqueous sample is delivered from the continuous channel.

Fig. 2(*c*) shows a microscopy image of a Y-junction device printed in PETA-B. As the aqueous phase, we used either the mother liquor alone or the mother liquor containing PSII crystals. In these three images [Figs. 2(*a*)–2(*c*)], the interface between the two immiscible fluids can be clearly observed. To characterize the co-flow, the width of the aqueous stream (the distance measured from the 3D-printed capillary wall to the interface of the two co-flowing liquids) was determined at a defined position after the intersection, as outlined in the *Methods* section. Generally, the thickness of the aqueous flow stream decreases with increasing flow-rate ratio (Q_o/Q_a) for each of the geometries and resins, as one would expect from the corresponding volume fractions.

In Fig. 2(*d*), the thickness within the T-junction was investigated with PSII crystals, ranging from 5 to 25 µm, suspended in dehydration buffer (mother liquor) at varying flow-rate ratios. The same experiment was performed with just the dehydration buffer to identify any effects originating from the crystals in the solution. The two experiments show comparable results, indicating that the co-flow thickness is not disturbed by the presence of crystals in the crystal size range explored.

In addition, a numerical model was established (see *Methods* section) in which the parameters of the oil and aqueous phases were adapted to the liquids used and the properties of the device resin, as outlined in the supporting information, Table S1. The two phases were introduced from the inlets defined in the model with matching geometry of the T-junction and formed a well defined co-flow, as illustrated in Fig. S1, similarly to Figs. 2(*a*)–2(*c*). Variations in the co-flow widths were measured using the *ImageJ* software (Schneider *et al.*, 2012), similarly to the experimental case, and are plotted in Fig. 2(*d*) for the T-geometry and PSII dehydration buffer. The simulations are in excellent agreement with the experimental results obtained for the co-flow thickness.

The 90° angle in the T-junction geometry [Figs. 2(*a*) and 2(*d*)] proved to be challenging, with crystals building up during hours-long XFEL experiments and eventually leading to clogging. Therefore, a smoother transition design was created with a 45° angle between the two channels forming the intersection, termed a Y-junction. To alleviate clogging challenges further, the two different sample configuration modes were investigated. Figs. 2(*e*) and 2(*f*) show the comparison of these two modes in the Y-junction device. Note that data presented in Fig. 2(*e*) correspond to 3D-printed Y-junctions fabricated with IP-S photoresist and data in Fig. 2(*f*) were

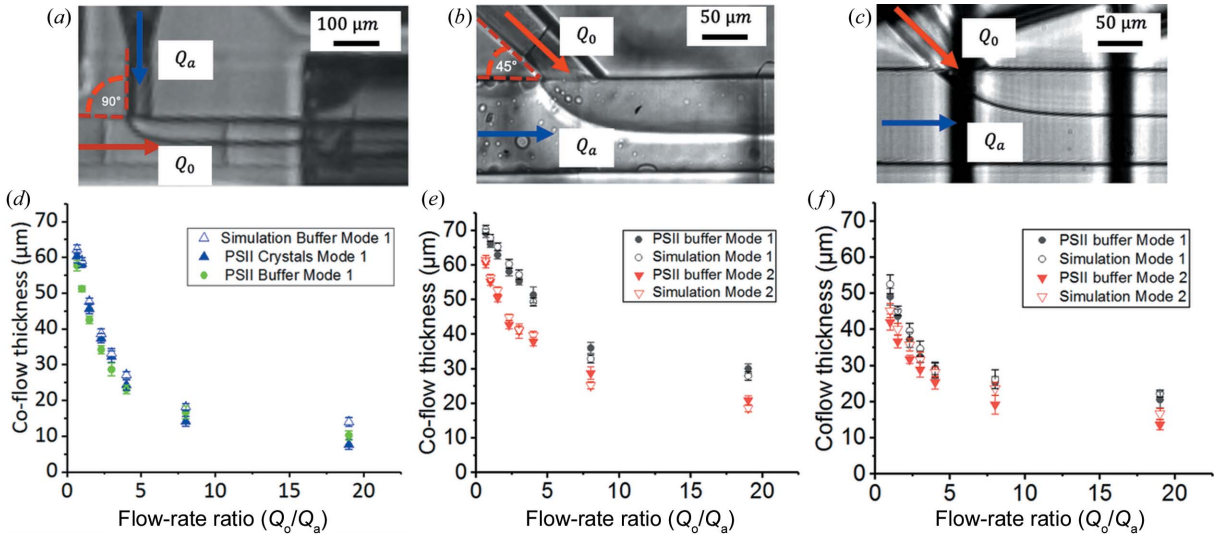

Figure 2
(*a*) Bright-field microscopy image of the T-junction geometry 3D-printed with IP-S photoresist in mode 1 with a flow-rate ratio of 1. (*b*) Bright-field microscopy image of the Y-junction geometry 3D-printed with IP-S photoresist in mode 2 with a flow-rate ratio of 4. (*c*) Bright-field microscopy image of the Y-junction geometry 3D-printed with PETA-B photoresist in mode 2 with a flow-rate ratio of 1. (*d*) Co-flow thickness of the T-junction device with PSII crystal in the buffer (filled green circles), PSII buffer only (filled blue triangles) and simulation (open blue triangles). The error bars indicate the standard deviation of the co-flow thickness. The devices used to test these conditions were made of IP-S photoresist. (*e*) The co-flow thickness of the Y-junction with PSII buffer in mode 1 (filled black circles) and mode 2 (filled red triangles) compared with the numerical simulation in mode 1 (open black circles) and simulation mode 2 (open red triangles). The error bars indicate the standard deviation of the co-flow thickness. The devices used to test these conditions were made of IP-S photoresist. (*f*) The co-flow thickness of the Y-junction with PSII buffer in mode 1 (filled black circles) and mode 2 (filled red triangles) compared with simulation mode 1 (open black circles) and simulation mode 2 (open red triangles). The error bars indicate the standard deviation of the co-flow thickness. The devices used to test these conditions were made of PETA-B photoresist.

obtained with a device made of PETA-B. As for the T-junction geometry, the thickness of the aqueous flow decreases with increasing flow-rate ratio for both device resins.

The co-flow thickness in the IP-S device differs considerably in the two modes, as a smaller co-flow thickness (width of the aqueous phase) is apparent over all probed flow-rate ratios. This trend was also confirmed in the numerical model data. This phenomenon could be caused by the aqueous sample entering the continuous channel at a larger diameter (100 µm) in mode 2 than in mode 1 (75 µm). Overall, a similar trend to the IP-S co-flow characterization was observed by the Y-junction fabricated with PETA-B photoresist. No significant differences were observed between the two design modes, either experimentally or in the simulation.

Since co-flow conditions were observed up to a flow-rate ratio of 19, for the devices tested in Fig. 3 we conclude that the sample consumption can be reduced by about 95% with this method.

While the crystals employed in this work, with sizes of the order of tens of micrometres, required flow-rate ratios of 3 or lower to be fully encapsulated in their mother liquor, it is hypothesized that nanocrystalline slurries and such with crystal sizes up to 5 µm would be comfortably suspended in their injection solution when the ratios meet the explored limit of 19 as this ratio leads to a co-flow thickness of 10 µm [see Figs. 2(*d*)–2(*f*)]. However, limitations for SFX experiments need to be taken into account, such as clogging, which is enhanced at very low sample flow rates, and decreased hit rates, which may occur given high dilution with the oil phase in the extreme-flow-rate-ratio cases. In addition, the viscosity of the sample medium poses further limitations in jetting samples with GDVNs, although these can be overcome with co-flow injection, as indicated below.

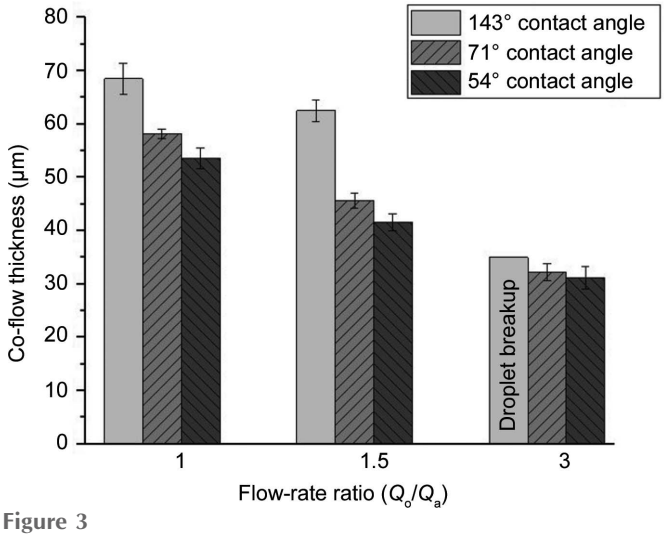

Figure 3
Co-flow thickness in the T-junction with PSII buffer in mode 1 at different flow rates and contact angles. Co-flow thickness was estimated for contact angles of 143, 71 and 54°. The co-flow thickness decreases with decreasing contact angle. For a flow-rate ratio of 3, instead of co-flow, droplet generation was observed for a hydrophobic condition (contact angle of 143°). The error bars indicate the standard deviation of the co-flow thickness.

The co-flow thickness depends not only on the device geometry and mode but also on the surface properties of the devices, most notably the wetting properties. When two immiscible fluids and a solid interface are in contact with each other, there is an inward-directed force that attempts to minimize the contact with the surface by pulling one of the liquids into the shape of a sphere. The resultant angle between the interface of the two fluids and the solid layer is a function of the specific free energy of the interface, where the interfacial tension forces between all three phases can be related to the contact angle (θ) of the surface (Tiab & Donaldson, 2012; Rowlinson & Windom, 1982). This contact angle depends on the two liquids used and the characteristics of the surface of the solid.

In our case, we observed that surfaces printed with IP-S photoresist showed significant changes in the contact angle and thus in the wetting properties over time. A shift from hydrophobic to hydrophilic surface properties over time was observed for both the IP-S and PETA-B surfaces. As demonstrated in Fig. S5, the contact angle drops significantly for IP-S surfaces over a period of two weeks from hydrophobic (∼140°) to hydrophilic (below 80°), as assessed with the sessile drop method. Over a similar time scale, the PETA-B surfaces showed a comparable trend, although the contact angle change due to to wetting properties is less pronounced. Since devices are usually fabricated days or weeks in advance of XFEL experiments, we therefore repeated the numerical simulations with three different resin contact angles for three Q_o and Q_a while maintaining Q_{tot} at 20 µl min^{-1}. Fig. 3 displays the obtained co-flow width for mode 1 in a T-junction device. For each tested flow-rate ratio, the thickness of the aqueous flow stream decreases when the contact angle decreases (*i.e.* when the material becomes increasingly hydrophilic). For a flow-rate ratio of 3 (Q_o of 15 µl min^{-1} and Q_a of 5 µl min^{-1}) on the most hydrophilic surface with a contact angle of 54°, the co-flow began to break up into droplets. Fig. S3 demonstrates the co-flow formation for the lower flow-rate ratios and droplet breakup at the largest flow-rate ratio as obtained from the numerical model. Thus, the variation in surface properties of the co-flow device material determines to a great extent when stable co-flow conditions prevail. In addition, we note that the experiments carried out at the EuXFEL were performed with devices that were produced and assembled several weeks in advance of the experiment, thus exhibiting hydrophilic surface properties, which generated stable co-flow in the SPB/SFX chamber, as shown next. The most extreme case with a contact angle of 54° may be avoided when devices are prepared less than two weeks in advance.

The co-flow devices were utilized at the EuXFEL during beamtime P2326. Fig. 4(*a*) shows the T-junction hybrid device coupled with a GDVN in the vacuum chamber of the SPB/SFX instrument with co-flow established (yellow arrow) and a jet that was approximately 600 µm in length, which is twice the length of a water jet at the same flow rate (Nazari *et al.*, 2020). Having a sufficiently fast jet is imperative because the sample must be replenished after being vaporized by the destructive

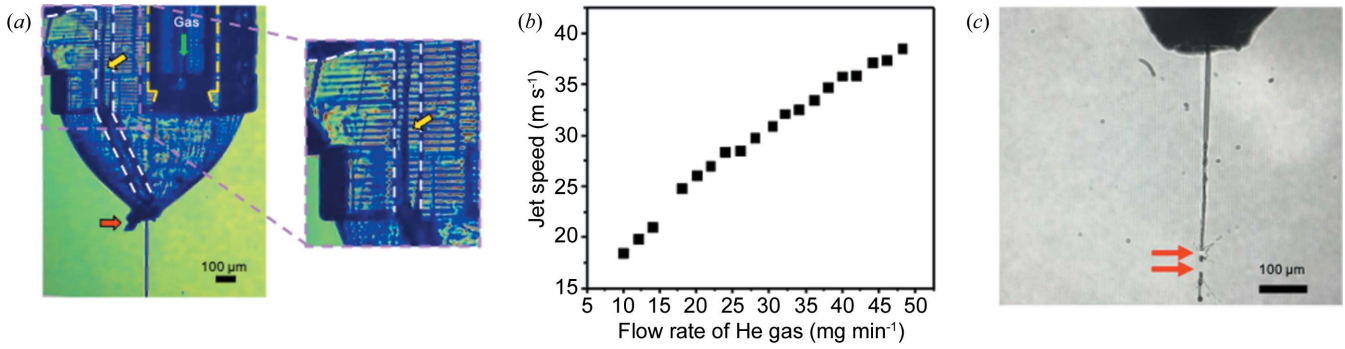

Figure 4
(*a*) An image of an IP-S co-flow device installed in the SPB/SFX chamber at the EuXFEL. The enlarged image shows the boundary of the two immiscible phases indicated by the yellow arrow. (*b*) Jet speed versus flow rate of He gas as investigated for PSII buffer obtained from a PETA-B co-flow hybrid. (*c*) Optical microscopy image of a jet containing protein crystals recorded in the SPB/SFX chamber (Q_o of 15 µl min^{-1}, Q_a of 5 µl min^{-1} and He flow rate of 20 mg min^{-1}). Jet imaging was performed by optical laser illumination after the second X-ray pulse in the bunch train to achieve this image. Highlighted with red arrows are the positions of where consecutive XFEL pulses impact the jet.

femtosecond X-ray pulses delivered at a megahertz repetition rate. Prior to the XFEL experiments, the jet speed was measured using methods published previously (Nazari *et al.*, 2020), based on the He mass flow applied to the GDVN, as shown in Fig. 4(*b*). The jet speed was analysed while exhibiting co-flow at a total liquid flow rate of 20 µl min^{-1} (Q_o = 15 µl min^{-1} and Q_a = 5 µl min^{-1}), which was the flow rate typically used when injecting with a GDVN-style nozzle.

In the SPB/SFX chamber, Q_{tot} = 20 µl min^{-1} and 20 mg min^{-1} of He were employed, and thus the jet speed was approximately 25.5 m s^{-1}. At this gas flow rate, two jet dissections caused by two X-ray pulses can be observed [Fig. 4(*c*)], indicating that the jet is fast enough to replenish the sample between X-ray pulses (spaced by 1.77 µs). This image relates to a co-flowing sample originating from a Y-junction device extruding a stable jet of the sample from the nozzle tip of the hybrid device. The upper red arrow in the image points to the location where the X-rays dissect the jet; the bottom arrow points to a spot just downstream where the 'hole' from the previous X-ray interaction point is clearly visible. This result is significant because a previous report (Wiedorn *et al.*, 2018) suggested that a minimum jet speed of 50 m s^{-1} was needed to replenish the sample between X-ray pulses at 1.1 MHz. With a repetition rate of 564 kHz, our results indicate that sample replenishing was achieved at about half that speed under co-flow injection conditions.

Due to the tremendous success in elucidating light-driven reactions with serial crystallography (Orville, 2020) it is also important to investigate whether new injection devices are compatible with the laser power and the typical wavelength ranges used for these experiments. We therefore tested both 3D-printed device materials for stability with a 532 nm nanosecond pump laser, which corresponds to the wavelength used to excite PSII to initiate the light-induced water oxidation reaction in the photosynthesis process (Kupitz *et al.*, 2014). To mimic the laser intensities used on the SPB/SFX instrument at the EuXFEL for TR experiments with PSII crystals, we subjected the 3D-printed devices to various laser powers and illumination times at a frequency of 10 Hz, corresponding to the pump laser frequency employed at the EuXFEL. As an example, Fig. 5 compares PETA-B devices before and after laser illumination in air at the highest power tested. No visible damage has occurred after 10 min of exposure at 360 mJ cm^{-2}. In contrast, the IP-S device showed

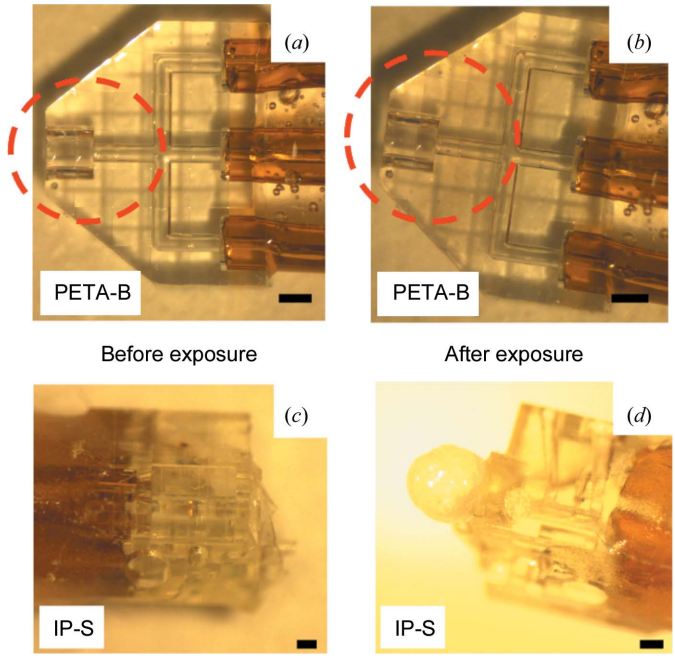

Figure 5
(*a*), (*b*) An exposure test of a 3D-printed PETA-B device (for demonstration purposes, a microfluidic mixer with similar device thickness and channel cross section to the co-flow hybrid devices) with a nanosecond 532 nm laser at 360 mJ cm^{-2} fluence in air for 10 min. The beam diameter was 1 mm and it was aligned over the device, as indicated by the red dashed circle corresponding approximately to the overlap spot in the EuXFEL experiment (with a distance of 800 µm from the nozzle tip into the device overlapping with the circular laser spot). (*b*) No visible damage was observed after laser illumination. (*c*), (*d*) A 3D-printed IP-S injection device (for demonstration purposes, a microfluidic droplet generator with similar device thickness and channel cross section to the co-flow hybrid devices) was employed for testing. Representative images are shown of IP-S devices (*c*) before and (*d*) after laser exposure (200 mJ cm^{-2} for 15 min). The IP-S devices show bubble formation at the nozzle exit of the device, indicating damage after laser illumination. Scale bars represent 200 µm in panels (*a*)–(*d*).

considerable degradation after 200 mJ cm^{-2} for 15 min, which could be attributed to heating effects and/or photochemical effects.

The robustness of the 3D-printed PETA-B co-flow hybrid devices was further substantiated through their use at the EuXFEL. They could be used for hours of operation in the SPB/SFX chamber in vacuum with the pump laser illuminating them for TR-SFX studies. Furthermore, diffraction was recorded for PSII crystals injected in co-flow mode at Q_o of 15 µl min^{-1} and Q_a of 5 µl min^{-1}. A representative diffraction pattern of PSII to a resolution above 5 Å is shown in Fig. 6.

Finally, we discuss the injection of highly viscous samples using the co-flow/GDVN hybrid devices during XFEL serial crystallography experiments in comparison with traditional GDVNs, which are still a highly attractive injection method in serial crystallography. Traditional nozzle life is strongly dependent on the samples injected, since highly viscous or concentrated samples tend to clog them within hours. This was also observed in our experiments. Employing 3D-printed GDVNs injecting crystals in dehydration buffer, jets could be run on average for 1 h before clogging effects became apparent (data not shown). In contrast, the 3D-printed hybrid co-flow devices lasted about 3.5 h (on average), which can be attributed to the addition of fluorinated oils to the system. The oil phase serves as a lubricant inside the microfluidic device, preventing crystals from agglomerating on the channel walls and clogging, and preventing the formation of irregularly shaped deposits of salt or polymer precipitations at the nozzle tip. Creating co-flow, however, dilutes the total volume of sample for injection, reducing the crystal concentration in the jet. This disadvantage is counteracted by the above-discussed improvements in injector lifetime, reducing the need to change injectors during beamtime and thus saving valuable experimentation time at XFEL instruments. Diluted crystal concentrations due to co-flow injection can also be counteracted with higher crystal densities.

An additional advantage of injection using co-flow is the ability to inject very high viscosity buffers, which would otherwise require extremely high pressures during the injection. For the PSII dehydration buffer employed in this study, a viscosity of 16.4 cP was determined (as a comparison, room-temperature water has a viscosity of 1 cP). At this viscosity, and with 2 m capillaries connecting from the reservoir to the nozzle, the pressure required to drive the sample to the nozzle within our devices ranged from 100 to 600 psi, dependent on the set flow rate. This is much lower than viscous injection with GDVNs without a co-flow injector, where typically pressures above 1000 psi are required.

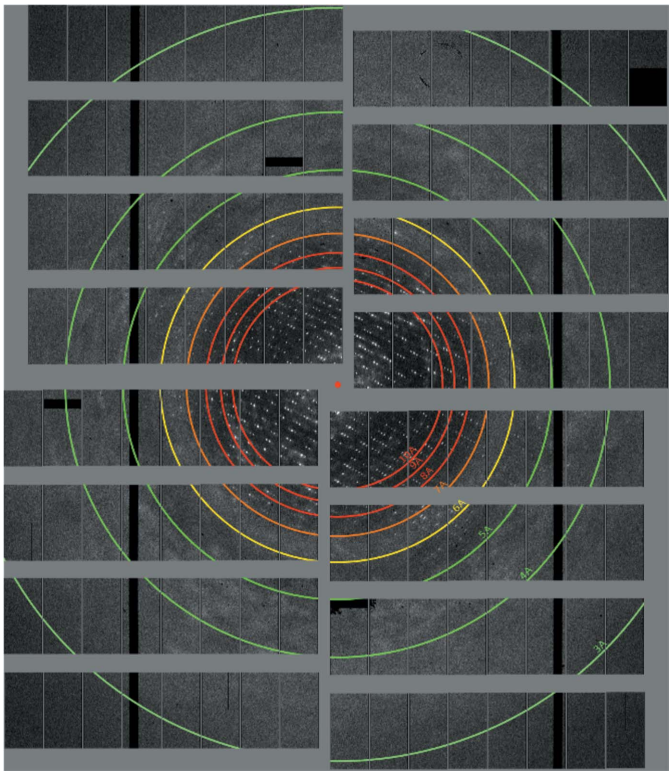

Figure 6
A representative diffraction pattern of PSII crystals delivered with the 3D-printed PETA-B co-flow hybrid device with a resolution better than 5 Å.

4. Conclusions

We have developed and characterized novel 3D-printed co-flow injection devices for serial crystallography experiments at XFELs. These devices are robust and can be readily fabricated as hybrid devices coupled to GDVNs with high-resolution 3D-printing technology. Both the commercial resin IP-S and the triacrylate resin PETA-B reliably generated co-flow, allowing a reduction in sample flow rates of a highly viscous sample buffer for SFX experiments at XFELs to 1 µl min^{-1}, which translates to about 95% less sample slurry injected. The devices can jet highly viscous buffers and co-flowing oil phase, generating long jets which are advantageous for positioning the XFEL interaction region far from the nozzle tip to reduce degradation. The devices also show lubricating effects, similar to droplet devices using the same oils (Echelmeier *et al.*, 2019, 2020; Pandey *et al.*, 2020), and could be operated on average three to four times longer than regular GDVNs with the same buffers, sometimes lasting full shifts (12 h) at the EuXFEL without severe clogging. This leads to a more effective use of available beamtime, as nozzle exchange times where no data can be collected are avoided. This advantage can offset potential disadvantages due to dilution effects with the co-flowing oil. In addition, the PETA-B devices exhibit minimal light absorbance in the visible wavelength range and are therefore suited for TR-SFX when light-induced reactions are studied at XFELs. This was verified in device fatigue measurements with conditions mimicking laser illumination during SFX experiments and during TR-SFX at the EuXFEL with PSII crystals. Finally, the co-flow injectors presented here were fabricated with high-resolution 3D-printing technology, which will further allow the integration of microfluidic mixers upstream from the co-flow generation region through fairly simple design adaptations similar to the 3D-printed mixers used in TR-SFX experiments in the past (Ishigami *et al.*, 2018).

These co-flow injectors could therefore play an important role in TR-SFX experiments with XFELs in the future.

Acknowledgements

We acknowledge the European XFEL in Schenefeld, Germany, for provision of X-ray free-electron laser beamtime on Scientific Instrument SPB/SFX (Single Particles, Clusters and Biomolecules, and Serial Femtosecond Crystallography) and would like to thank the instrument group and facility staff for their assistance. Dr Don Seo is gratefully acknowledged for providing access to the viscometer. Author contributions are as follows. Conceived experiment: AR, PF; planned experiments: AR, PF, NZ, RAK, TG, DD, MTR, SG; developed co-flow injector: AR, JCV, DD, DHK, SG, RN, RAK, SZa, MSo; executed SFX experiment: RL, AR, PF, RF, FHMK, NZ, BDB, DD, MOW, VMaz, JB, RdW, PV, ARR, MK, MV, MF, RCA, KK, JM, MM, MSc, TS; responsible SPB/SFX instrument scientist: RL; led development of SPB/SFX instrument: APM; contributed to SPB/SFX instrument development: MOW, JK, SBa, MY, HNC, APM, RL, JB, RdW, ARR, PV, TS; prepared crystal sample: FHMK, JM, JDMA, PF, RF, JMMG, JY, MLS, MAC, TLO, KM, ED, ZD, JDZ, BDB, JN, JDMA, MSc, CK; set up and tested optical laser: RL, SV, GK, TS; contributed to experiment preparation: DHK, JCV, AEG, MS, UW, JCHS, SS, MY, MSH, RN, SZh, MSo; analysed diffraction data: SBo, NZ, RAK, NES, PS, AO, AH; developed numerical model: MTR, AR; analysed co-flow data: DD, MTR, SG, AR; contributed to online data processing: AB, TG, JC, VMar, RAK, NZ, GKK, NES, SBo; wrote manuscript: AR, DD, MTR with input from all other co-authors.

Funding information

Financial support from the STC Program of the US National Science Foundation through BioXFEL (agreement No. 1231306), NSF ABI Innovations (award No. 1565180), NSF CAREER (award No. 1943448) and NSF MCB (award No. 1817862), and from the National Institutes of Health (award No. R01GM095583 and award No. S10OD021816-01 entitled '3D Nanoprinter') is gratefully acknowledged. The development of the underlying algorithms was supported by the US Department of Energy, Office of Science, Basic Energy Sciences (award No. DE-SC0002164; underlying dynamic techniques), and by the NSF (award No. 1231306; underlying data analytical techniques). The work was also supported by the Biodesign Center for Applied Structural Discovery at Arizona State University and by the Cluster of Excellence 'CUI: Advanced Imaging of Matter' of the Deutsche Forschungsgemeinschaft (DFG) (EXC 2056, project No. 390715994). GK and SMV were partially supported by the National Institutes of Health (grant No. R01GM120537).

References

Abramoff, M. D., Magalhaes, P. J. & Ram, S. J. (2004). *Biophoton. Int.* **11**, 36–42.

Adrian, R. (1991). *Annu. Rev. Fluid Mech.* **23**, 261–304.

Allahgholi, A., Becker, J., Delfs, A., Dinapoli, R., Goettlicher, P., Greiffenberg, D., Henrich, B., Hirsemann, H., Kuhn, M., Klanner, R., Klyuev, A., Krueger, H., Lange, S., Laurus, T., Marras, A., Mezza, D., Mozzanica, A., Niemann, M., Poehlsen, J., Schwandt, J., Sheviakov, I., Shi, X., Smoljanin, S., Steffen, L., Sztuk-Dambietz, J., Trunk, U., Xia, Q., Zeribi, M., Zhang, J., Zimmer, M., Schmitt, B. & Graafsma, H. (2019). *J. Synchrotron Rad.* **26**, 74–82.

Ananyev, G., Roy-Chowdhury, S., Gates, C., Fromme, P. & Dismukes, G. C. (2019). *ACS Catal.* **9**, 1396–1407.

Atha, D. H. & Ingham, K. C. (1981). *J. Biol. Chem.* **256**, 12108–12117.

Bashir, S., Rees, J. M. & Zimmerman, W. B. (2011). *Chem. Eng. Sci.* **66**, 4733–4741.

Bean, R. J., Aquila, A., Samoylova, L. & Mancuso, A. P. (2016). *J. Opt.* **18**, 074011.

Boukhelef, D., Szuba, J., Wrona, K. & Youngman, C. (2013). *Proceedings of ICALEPCS 2013*, San Francisco, 6–11 October 2013, Abstract No. TUPPC045, pp. 665–668. Geneva: JACoW.

Boutet, S., Lomb, L., Williams, G. J., Barends, T. R. M., Aquila, A., Doak, R. B., Weierstall, U., DePonte, D. P., Steinbrener, J., Shoeman, R. L., Messerschmidt, M., Barty, A., White, T. A., Kassemeyer, S., Kirian, R. A., Seibert, M. M., Montanez, P. A., Kenney, C., Herbst, R., Hart, P., Pines, J., Haller, G., Gruner, S. M., Philipp, H. T., Tate, M. W., Hromalik, M., Koerner, L. J., van Bakel, N., Morse, J., Ghonsalves, W., Arnlund, D., Bogan, M. J., Caleman, C., Fromme, R., Hampton, C. Y., Hunter, M. S., Johansson, L. C., Katona, G., Kupitz, C., Liang, M. N., Martin, A. V., Nass, K., Redecke, L., Stellato, F., Timneanu, N., Wang, D. J., Zatsepin, N. A., Schafer, D., Defever, J., Neutze, R., Fromme, P., Spence, J. C. H., Chapman, H. N. & Schlichting, I. (2012). *Science*, **337**, 362–364.

Bückmann, T., Stenger, N., Kadic, M., Kaschke, J., Frölich, A., Kennerknecht, T., Eberl, C., Thiel, M. & Wegener, M. (2012). *Adv. Mater.* **24**, 2710–2714.

Calvey, G. D., Katz, A. M., Schaffer, C. B. & Pollack, L. (2016). *Struct. Dyn.* **3**, 054301.

Chapman, H. N., Fromme, P., Barty, A., White, T. A., Kirian, R. A., Aquila, A., Hunter, M. S., Schulz, J., DePonte, D. P., Weierstall, U., Doak, R. B., Maia, F., Martin, A. V., Schlichting, I., Lomb, L., Coppola, N., Shoeman, R. L., Epp, S. W., Hartmann, R., Rolles, D., Rudenko, A., Foucar, L., Kimmel, N., Weidenspointner, G., Holl, P., Liang, M. N., Barthelmess, M., Caleman, C., Boutet, S., Bogan, M. J., Krzywinski, J., Bostedt, C., Bajt, S., Gumprecht, L., Rudek, B., Erk, B., Schmidt, C., Hömke, A., Reich, C., Pietschner, D., Strüder, L., Hauser, G., Gorke, H., Ullrich, J., Herrmann, S., Schaller, G., Schopper, F., Soltau, H., Kühnel, K. U., Messerschmidt, M., Bozek, J. D., Hau-Riege, S. P., Frank, M., Hampton, C. Y., Sierra, R. G., Starodub, D., Williams, G. J., Hajdu, J., Timneanu, N., Seibert, M. M., Andreasson, J., Rocker, A., Jönsson, O., Svenda, M., Stern, S., Nass, K., Andritschke, R., Schröter, C. D., Krasniqi, F., Bott, M., Schmidt, K. E., Wang, X. Y., Grotjohann, I., Holton, J. M., Barends, T. R. M., Neutze, R., Marchesini, S., Fromme, R., Schorb, S., Rupp, D., Adolph, M., Gorkhover, T., Andersson, I., Hirsemann, H., Potdevin, G., Graafsma, H., Nilsson, B. & Spence, J. C. H. (2011). *Nature*, **470**, 73–77.

Conrad, C. E., Basu, S., James, D., Wang, D., Schaffer, A., Roy-Chowdhury, S., Zatsepin, N. A., Aquila, A., Coe, J., Gati, C., Hunter, M. S., Koglin, J. E., Kupitz, C., Nelson, G., Subramanian, G., White, T. A., Zhao, Y., Zook, J., Boutet, S., Cherezov, V., Spence, J. C. H., Fromme, R., Weierstall, U. & Fromme, P. (2015). *IUCrJ*, **2**, 421–430.

Decking, W., Abeghyan, S., Abramian, P., Abramsky, A., Aguirre, A., Albrecht, C., Alou, P., Altarelli, M., Altmann, P., Amyan, K., Anashin, V., Apostolov, E., Appel, K., Auguste, D., Ayvazyan, V., Baark, S., Babies, F., Baboi, N., Bak, P., Balandin, V., Baldinger, R., Baranasic, B., Barbanotti, S., Belikov, O., Belokurov, V., Belova, L., Belyakov, V., Berry, S., Bertucci, M., Beutner, B., Block, A., Blöcher, M., Böckmann, T., Bohm, C., Böhnert, M., Bondar, V., Bondarchuk, E., Bonezzi, M., Borowiec, P., Bösch, C., Bösenberg, U., Bosotti, A., Böspflug, R., Bousonville, M., Boyd, E., Bozhko, Y.,

Brand, A., Branlard, J., Briechle, S., Brinker, F., Brinker, S., Brinkmann, R., Brockhauser, S., Brovko, O., Brück, H., Brüdgam, A., Butkowski, L., Büttner, T., Calero, J., Castro-Carballo, E., Cattalanotto, G., Charrier, J., Chen, J., Cherepenko, A., Cheskidov, V., Chiodini, M., Chong, A., Choroba, S., Chorowski, M., Churanov, D., Cichalewski, W., Clausen, M., Clement, W., Cloué, C., Cobos, J. A., Coppola, N., Cunis, S., Czuba, K., Czwalinna, M., D'Almagne, B., Dammann, J., Danared, H., de Zubiaurre Wagner, A., Delfs, A., Delfs, T., Dietrich, F., Dietrich, T., Dohlus, M., Dommach, M., Donat, A., Dong, X., Doynikov, N., Dressel, M., Duda, M., Duda, P., Eckoldt, H., Ehsan, W., Eidam, J., Eints, F., Engling, C., Englisch, U., Ermakov, A., Escherich, K., Eschke, J., Saldin, E., Faesing, M., Fallou, A., Felber, M., Fenner, M., Fernandes, B., Fernández, J. M., Feuker, S., Filippakopoulos, K., Floettmann, K., Fogel, V., Fontaine, M., Francés, A., Martin, I. F., Freund, W., Freyermuth, T., Friedland, M., Fröhlich, L., Fusetti, M., Fydrych, J., Gallas, A., García, O., Garcia-Tabares, L., Geloni, G., Gerasimova, N., Gerth, C., Geßler, P., Gharibyan, V., Gloor, M., Głowinkowski, J., Goessel, A., Gołębiewski, Z., Golubeva, N., Grabowski, W., Graeff, W., Grebentsov, A., Grecki, M., Grevsmuehl, T., Gross, M., Grosse-Wortmann, U., Grünert, J., Grunewald, S., Grzegory, P., Feng, G., Guler, H., Gusev, G., Gutierrez, J. L., Hagge, L., Hamberg, M., Hanneken, R., Harms, E., Hartl, I., Hauberg, A., Hauf, S., Hauschildt, J., Hauser, J., Havlicek, J., Hedqvist, A., Heidbrook, N., Hellberg, F., Henning, D., Hensler, O., Hermann, T., Hidvégi, A., Hierholzer, M., Hintz, H., Hoffmann, F., Hoffmann, M., Hoffmann, M., Holler, Y., Hüning, M., Ignatenko, A., Ilchen, M., Iluk, A., Iversen, J., Iversen, J., Izquierdo, M., Jachmann, L., Jardon, N., Jastrow, U., Jensch, K., Jensen, J., Jeżabek, M., Jidda, M., Jin, H., Johansson, N., Jonas, R., Kaabi, W., Kaefer, D., Kammering, R., Kapitza, H., Karabekyan, S., Karstensen, S., Kasprzak, K., Katalev, V., Keese, D., Keil, B., Kholopov, M., Killenberger, M., Kitaev, B., Klimchenko, Y., Klos, R., Knebel, L., Koch, A., Koepke, M., Köhler, S., Köhler, W., Kohlstrunk, N., Konopkova, Z., Konstantinov, A., Kook, W., Koprek, W., Körfer, M., Korth, O., Kosarev, A., Kosiński, K., Kostin, D., Kot, Y., Kotarba, A., Kozak, T., Kozak, V., Kramert, R., Krasilnikov, M., Krasnov, A., Krause, B., Kravchuk, L., Krebs, O., Kretschmer, R., Kreutzkamp, J., Kröplin, O., Krzysik, K., Kube, G., Kuehn, H., Kujala, N., Kulikov, V., Kuzminych, V., La Civita, D., Lacroix, M., Lamb, T., Lancetov, A., Larsson, M., Le Pinvidic, D., Lederer, S., Lensch, T., Lenz, D., Leuschner, A., Levenhagen, F., Li, Y., Liebing, J., Lilje, L., Limberg, T., Lipka, D., List, B., Liu, J., Liu, S., Lorbeer, B., Lorkiewicz, J., Lu, H. H., Ludwig, F., Machau, K., Maciocha, W., Madec, C., Magueur, C., Maiano, C., Maksimova, I., Malcher, K., Maltezopoulos, T., Mamoshkina, E., Manschwetus, B., Marcellini, F., Marinkovic, G., Martinez, T., Martirosyan, H., Maschmann, W., Maslov, M., Matheisen, A., Mavric, U., Meißner, J., Meissner, K., Messerschmidt, M., Meyners, N., Michalski, G., Michelato, P., Mildner, N., Moe, M., Moglia, F., Mohr, C., Mohr, S., Möller, W., Mommerz, M., Monaco, L., Montiel, C., Moretti, M., Morozov, I., Morozov, P., Mross, D., Mueller, J., Müller, C., Müller, J., Müller, K., Munilla, J., Münnich, A., Muratov, V., Napoly, O., Näser, B., Nefedov, N., Neumann, R., Neumann, R., Ngada, N., Noelle, D., Obier, F., Okunev, I., Oliver, J. A., Omet, M., Oppelt, A., Ottmar, A., Oublaid, M., Pagani, C., Paparella, R., Paramonov, V., Peitzmann, C., Penning, J., Perus, A., Peters, F., Petersen, B., Petrov, A., Petrov, I., Pfeiffer, S., Pflüger, J., Philipp, S., Pienaud, Y., Pierini, P., Pivovarov, S., Planas, M., Pławski, E., Pohl, M., Polinski, J., Popov, V., Prat, S., Prenting, J., Priebe, G., Pryschelski, H., Przygoda, K., Pyata, E., Racky, B., Rathjen, A., Ratuschni, W., Regnaud-Campderros, S., Rehlich, K., Reschke, D., Robson, C., Roever, J., Roggli, M., Rothenburg, J., Rusiński, E., Rybaniec, R., Sahling, H., Salmani, M., Samoylova, L., Sanzone, D., Saretzki, F., Sawlanski, O., Schaffran, J., Schlarb, H., Schlösser, M., Schlott, V., Schmidt, C., Schmidt-Foehre, F., Schmitz, M., Schmökel, M., Schnautz, T., Schneidmiller, E., Scholz, M., Schöneburg, B., Schultze, J., Schulz, C., Schwarz, A., Sekutowicz, J., Sellmann, D., Semenov, E., Serkez, S., Sertore, D., Shehzad, N., Shemarykin, P., Shi, L., Sienkiewicz, M., Sikora, D., Sikorski, M., Silenzi, A., Simon, C., Singer, W., Singer, X., Sinn, H., Sinram, K., Skvorodnev, N., Smirnow, P., Sommer, T., Sorokin, A., Stadler, M., Steckel, M., Steffen, B., Steinhau-Kühl, N., Stephan, F., Stodulski, M., Stolper, M., Sulimov, A., Susen, R., Świerblewski, J., Sydlo, C., Syresin, E., Sytchev, V., Szuba, J., Tesch, N., Thie, J., Thiebault, A., Tiedtke, K., Tischhauser, D., Tolkiehn, J., Tomin, S., Tonisch, F., Toral, F., Torbin, I., Trapp, A., Treyer, D., Trowitzsch, G., Trublet, T., Tschentscher, T., Ullrich, F., Vannoni, M., Varela, P., Varghese, G., Vashchenko, G., Vasic, M., Vazquez-Velez, C., Verguet, A., Vilcins-Czvitkovits, S., Villanueva, R., Visentin, B., Viti, M., Vogel, E., Volobuev, E., Wagner, R., Walker, N., Wamsat, T., Weddig, H., Weichert, G., Weise, H., Wenndorf, R., Werner, M., Wichmann, R., Wiebers, C., Wiencek, M., Wilksen, T., Will, I., Winkelmann, L., Winkowski, M., Wittenburg, K., Witzig, A., Wlk, P., Wohlenberg, T., Wojciechowski, M., Wolff-Fabris, F., Wrochna, G., Wrona, K., Yakopov, M., Yang, B., Yang, F., Yurkov, M., Zagorodnov, I., Zalden, P., Zavadtsev, A., Zavadtsev, D., Zhirnov, A., Zhukov, A., Ziemann, V., Zolotov, A., Zolotukhina, N., Zummack, F. & Zybin, D. (2020). *Nat. Photon.* **14**, 391–397.

DePonte, D. P., Weierstall, U., Schmidt, K., Warner, J., Starodub, D., Spence, J. C. H. & Doak, R. B. (2008). *J. Phys. D Appl. Phys.* **41**, 195505.

Deshpande, K. B. & Zimmerman, W. B. (2006). *Chem. Eng. Sci.* **61**, 6486–6498.

Durbin, S. D. & Feher, G. (2017). *Methods Mol. Biol.* **1607**, 17–50.

Echelmeier, A., Cruz Villarreal, J., Messerschmidt, M., Kim, D., Coe, J. D., Thifault, D., Botha, S., Egatz-Gomez, A., Gandhi, S., Brehm, G., Conrad, C. E., Hansen, D. T., Madsen, C., Bajt, S., Meza-Aguilar, J. D., Oberthür, D., Wiedorn, M. O., Fleckenstein, H., Mendez, D., Knoška, J., Martin-Garcia, J. M., Hu, H., Lisova, S., Allahgholi, A., Gevorkov, Y., Ayyer, K., Aplin, S., Ginn, H. M., Graafsma, H., Morgan, A. J., Greiffenberg, D., Klujev, A., Laurus, T., Poehlsen, J., Trunk, U., Mezza, D., Schmidt, B., Kuhn, M., Fromme, R., Sztuk-Dambietz, J., Raab, N., Hauf, S., Silenzi, A., Michelat, T., Xu, C., Danilevski, C., Parenti, A., Mekinda, L., Weinhausen, B., Mills, G., Vagovic, P., Kim, Y., Kirkwood, H., Bean, R., Bielecki, J., Stern, S., Giewekemeyer, K., Round, A. R., Schulz, J., Dörner, K., Grant, T. D., Mariani, V., Barty, A., Mancuso, A. P., Weierstall, U., Spence, J. C. H., Chapman, H. N., Zatsepin, N., Fromme, P., Kirian, R. A. & Ros, A. (2020). *Nat. Commun.* **11**, 4511.

Echelmeier, A., Kim, D., Cruz Villarreal, J., Coe, J., Quintana, S., Brehm, G., Egatz-Gomez, A., Nazari, R., Sierra, R. G., Koglin, J. E., Batyuk, A., Hunter, M. S., Boutet, S., Zatsepin, N., Kirian, R. A., Grant, T. D., Fromme, P. & Ros, A. (2019). *J. Appl. Cryst.* **52**, 997–1008.

Finlayson, B. A. (2006). *Introduction to Chemical Engineering Computing*, pp. 176–179. Hoboken: Wiley.

Fuller, F. D., Gul, S., Chatterjee, R., Burgie, E. S., Young, I. D., Lebrette, H., Srinivas, V., Brewster, A. S., Michels-Clark, T., Clinger, J. A., Andi, B., Ibrahim, M., Pastor, E., de Lichtenberg, C., Hussein, R., Pollock, C. J., Zhang, M., Stan, C. A., Kroll, T., Fransson, T., Weninger, C., Kubin, M., Aller, P., Lassalle, L., Bräuer, P., Miller, M. D., Amin, M., Koroidov, S., Roessler, C. G., Allaire, M., Sierra, R. G., Docker, P. T., Glownia, J. M., Nelson, S., Koglin, J. E., Zhu, D., Chollet, M., Song, S., Lemke, H., Liang, M., Sokaras, D., Alonso-Mori, R., Zouni, A., Messinger, J., Bergmann, U., Boal, A. K., Bollinger, J. M. Jr, Krebs, C., Högbom, M., Phillips, G. N. Jr, Vierstra, R. D., Sauter, N. K., Orville, A. M., Kern, J., Yachandra, V. K. & Yano, J. (2017). *Nat. Methods*, **14**, 443–449.

Gisriel, C., Coe, J., Letrun, R., Yefanov, O. M., Luna-Chavez, C., Stander, N. E., Lisova, S., Mariani, V., Kuhn, M., Aplin, S., Grant, T. D., Dörner, K., Sato, T., Echelmeier, A., Cruz Villarreal, J., Hunter, M. S., Wiedorn, M. O., Knoska, J., Mazalova, V., Roy-Chowdhury, S., Yang, J.-H., Jones, A., Bean, R., Bielecki, J., Kim, Y., Mills, G., Weinhausen, B., Meza, J. D., Al-Qudami, N., Bajt, S., Brehm, G., Botha, S., Boukhelef, D., Brockhauser, S., Bruce, B. D., Coleman, M. A., Danilevski, C., Discianno, E., Dobson, Z.,

Fangohr, H., Martin-Garcia, J. M., Gevorkov, Y., Hauf, S., Hosseinizadeh, A., Januschek, F., Ketawala, G. K., Kupitz, C., Maia, L., Manetti, M., Messerschmidt, M., Michelat, T., Mondal, J., Ourmazd, A., Previtali, G., Sarrou, I., Schön, S., Schwander, P., Shelby, M. L., Silenzi, A., Sztuk-Dambietz, J., Szuba, J., Turcato, M., White, T. A., Wrona, K., Xu, C., Abdellatif, M. H., Zook, J. D., Spence, J. C. H., Chapman, H. N., Barty, A., Kirian, R. A., Frank, M., Ros, A., Schmidt, M., Fromme, R., Mancuso, A. P., Fromme, P. & Zatsepin, N. A. (2019). *Nat. Commun.* **10**, 5021.

Grünbein, M. L., Bielecki, J., Gorel, A., Stricker, M., Bean, R., Cammarata, M., Dörner, K., Fröhlich, L., Hartmann, E., Hauf, S., Hilpert, M., Kim, Y., Kloos, M., Letrun, R., Messerschmidt, M., Mills, G., Nass Kovacs, G., Ramilli, M., Roome, C. M., Sato, T., Scholz, M., Sliwa, M., Sztuk-Dambietz, J., Weik, M., Weinhausen, B., Al-Qudami, N., Boukhelef, D., Brockhauser, S., Ehsan, W., Emons, M., Esenov, S., Fangohr, H., Kaukher, A., Kluyver, T., Lederer, M., Maia, L., Manetti, M., Michelat, T., Münnich, A., Pallas, F., Palmer, G., Previtali, G., Raab, N., Silenzi, A., Szuba, J., Venkatesan, S., Wrona, K., Zhu, J., Doak, R. B., Shoeman, R. L., Foucar, L., Colletier, J. P., Mancuso, A. P., Barends, T. R. M., Stan, C. A. & Schlichting, I. (2018). *Nat. Commun.* **9**, 3487.

Gusach, A., Maslov, I., Luginina, A., Borshchevskiy, V., Mishin, A. & Cherezov, V. (2020). *Curr. Opin. Struct. Biol.* **63**, 18–25.

Han, H., Round, E., Schubert, R., Gül, Y., Makroczyová, J., Meza, D., Heuser, P., Aepfelbacher, M., Barák, I., Betzel, C., Fromme, P., Kursula, I., Nissen, P., Tereschenko, E., Schulz, J., Uetrecht, C., Ulicný, J., Wilmanns, M., Hajdu, J., Lamzin, V. S. & Lorenzen, K. (2021). *J. Appl. Cryst.* **54**, 7–21.

Hunter, M. S., Segelke, B., Messerschmidt, M., Williams, G. J., Zatsepin, N. A., Barty, A., Benner, W. H., Carlson, D. B., Coleman, M., Graf, A., Hau-Riege, S. P., Pardini, T., Seibert, M. M., Evans, J., Boutet, S. & Frank, M. (2014). *Sci. Rep.* **4**, 6026.

Ishigami, I., Lewis-Ballester, A., Echelmeier, A., Brehm, G., Zatsepin, N., Grant, T., Coe, J., Lisova, S., Nelson, G., Zhang, S., Dobson, Z., Boutet, S. R. S., Batyuk, A., Fromme, P., Fromme, R. J. S., Ros, A., Yeh, S.-R. & Rousseau, D. (2018). *Proc. Natl Acad. Sci. USA*, **116**, 572–577.

James, D. (2015). Dissertation, Arizona State University, USA.

Kang, Y. Y., Zhou, X. E., Gao, X., He, Y. Z., Liu, W., Ishchenko, A., Barty, A., White, T. A., Yefanov, O., Han, G. W., Xu, Q. P., de Waal, P. W., Ke, J. Y., Tan, M. H. E., Zhang, C. H., Moeller, A., West, G. M., Pascal, B. D., Van Eps, N., Caro, L. N., Vishnivetskiy, S. A., Lee, R. J., Suino-Powell, K. M., Gu, X., Pal, K., Ma, J. M., Zhi, X. Y., Boutet, S., Williams, G. J., Messerschmidt, M., Gati, C., Zatsepin, N. A., Wang, D. J., James, D., Basu, S., Roy-Chowdhury, S., Conrad, C. E., Coe, J., Liu, H. G., Lisova, S., Kupitz, C., Grotjohann, I., Fromme, R., Jiang, Y., Tan, M. J., Yang, H. Y., Li, J., Wang, M. T., Zheng, Z., Li, D. F., Howe, N., Zhao, Y. M., Standfuss, J., Diederichs, K., Dong, Y. H., Potter, C. S., Carragher, B., Caffrey, M., Jiang, H. L., Chapman, H. N., Spence, J. C. H., Fromme, P., Weierstall, U., Ernst, O. P., Katritch, V., Gurevich, V. V., Griffin, P. R., Hubbell, W. L., Stevens, R. C., Cherezov, V., Melcher, K. & Xu, H. E. (2015). *Nature*, **523**, 561–567.

Kim, D., Echelmeier, A., Cruz Villarreal, J., Gandhi, S., Quintana, S., Egatz-Gomez, A. & Ros, A. (2019). *Anal. Chem.* **91**, 9792–9799.

Koua, F. H., Umena, Y., Kawakami, K. & Shen, J. R. (2013). *Proc. Natl Acad. Sci. USA*, **110**, 3889–3894.

Kupitz, C., Basu, S., Grotjohann, I., Fromme, R., Zatsepin, N. A., Rendek, K. N., Hunter, M. S., Shoeman, R. L., White, T. A., Wang, D., James, D., Yang, J.-H., Cobb, D. E., Reeder, B., Sierra, R. G., Liu, H., Barty, A., Aquila, A. L., Deponte, D., Kirian, R. A., Bari, S., Bergkamp, J. J., Beyerlein, K. R., Bogan, M. J., Caleman, C., Chao, T.-C., Conrad, C. E., Davis, K. M., Fleckenstein, H., Galli, L., Hau-Riege, S. P., Kassemeyer, S., Laksmono, H., Liang, M., Lomb, L., Marchesini, S., Martin, A. V., Messerschmidt, M., Milathianaki, D., Nass, K., Ros, A., Roy-Chowdhury, S., Schmidt, K., Seibert, M., Steinbrener, J., Stellato, F., Yan, L., Yoon, C., Moore, T. A., Moore, A. L., Pushkar, Y., Williams, G. J., Boutet, S., Doak, R. B., Weierstall, U., Frank, M., Chapman, H. N., Spence, J. C. H. & Fromme, P. (2014). *Nature*, **513**, 261–265.

Kupitz, C., Olmos, J. L. Jr, Holl, M., Tremblay, L., Pande, K., Pandey, S., Oberthür, D., Hunter, M., Liang, M., Aquila, A., Tenboer, J., Calvey, G., Katz, A., Chen, Y., Wiedorn, M. O., Knoska, J., Meents, A., Majriani, V., Norwood, T., Poudyal, I., Grant, T., Miller, M. D., Xu, W., Tolstikova, A., Morgan, A., Metz, M., Martin-Garcia, J. M., Zook, J. D., Roy-Chowdhury, S., Coe, J., Nagaratnam, N., Meza, D., Fromme, R., Basu, S., Frank, M., White, T., Barty, A., Bajt, S., Yefanov, O., Chapman, H. N., Zatsepin, N., Nelson, G., Weierstall, U., Spence, J., Schwander, P., Pollack, L., Fromme, P., Ourmazd, A., Phillips, G. N. Jr & Schmidt, M. (2017). *Struct. Dyn.* **4**, 044003.

Lomb, L., Steinbrener, J., Bari, S., Beisel, D., Berndt, D., Kieser, C., Lukat, M., Neef, N. & Shoeman, R. L. (2012). *J. Appl. Cryst.* **45**, 674–678.

Mafuné, F., Miyajima, K., Tono, K., Takeda, Y., Kohno, J., Miyauchi, N., Kobayashi, J., Joti, Y., Nango, E., Iwata, S. & Yabashi, M. (2016). *Acta Cryst.* D**72**, 520–523.

Mancuso, A. P., Aquila, A., Batchelor, L., Bean, R. J., Bielecki, J., Borchers, G., Doerner, K., Giewekemeyer, K., Graceffa, R., Kelsey, O. D., Kim, Y., Kirkwood, H. J., Legrand, A., Letrun, R., Manning, B., Lopez Morillo, L., Messerschmidt, M., Mills, G., Raabe, S., Reimers, N., Round, A., Sato, T., Schulz, J., Signe Takem, C., Sikorski, M., Stern, S., Thute, P., Vagovič, P., Weinhausen, B. & Tschentscher, T. (2019). *J. Synchrotron Rad.* **26**, 660–676.

Martin-Garcia, J. M., Conrad, C. E., Coe, J., Roy-Chowdhury, S. & Fromme, P. (2016). *Arch. Biochem. Biophys.* **602**, 32–47.

Mehrabi, P., Schulz, E. C., Agthe, M., Horrell, S., Bourenkov, G., von Stetten, D., Leimkohl, J.-P., Schikora, H., Schneider, T. R., Pearson, A. R., Tellkamp, F. & Miller, R. J. D. (2019). *Nat. Methods*, **16**, 979–982.

Middaugh, C. R., Tisel, W. A., Haire, R. N. & Rosenberg, A. (1979). *J. Biol. Chem.* **254**, 367–370.

Nazari, R., Zaare, S., Alvarez, R. C., Karpos, K., Engelman, T., Madsen, C., Nelson, G., Spence, J. C. H., Weierstall, U., Adrian, R. J. & Kirian, R. A. (2020). *Opt. Express*, **28**, 21749–21765.

Neutze, R., Wouts, R., van der Spoel, D., Weckert, E. & Hajdu, J. (2000). *Nature*, **406**, 752–757.

Oberthuer, D., Knoška, J., Wiedorn, M. O., Beyerlein, K. R., Bushnell, D. A., Kovaleva, E. G., Heymann, M., Gumprecht, L., Kirian, R. A., Barty, A., Mariani, V., Tolstikova, A., Adriano, L., Awel, S., Barthelmess, M., Dörner, K., Xavier, P. L., Yefanov, O., James, D. R., Nelson, G., Wang, D. J., Calvey, G., Chen, Y., Schmidt, A., Szczepek, M., Frielingsdorf, S., Lenz, O., Snell, E., Robinson, P. J., Šarler, B., Belšak, G., Maček, M., Wilde, F., Aquila, A., Boutet, S., Liang, M., Hunter, M. S., Scheerer, P., Lipscomb, J. D., Weierstall, U., Kornberg, R. D., Spence, J. C., Pollack, L., Chapman, H. N. & Bajt, S. (2017). *Sci. Rep.* **7**, 44628.

Olmos, J. L., Pandey, S., Martin-Garcia, J. M., Calvey, G., Katz, A., Knoska, J., Kupitz, C., Hunter, M. S., Liang, M., Oberthuer, D., Yefanov, O., Wiedorn, M., Heyman, M., Holl, M., Pande, K., Barty, A., Miller, M. D., Stern, S., Roy-Chowdhury, S., Coe, J., Nagaratnam, N., Zook, J., Verburgt, J., Norwood, T., Poudyal, I., Xu, D., Koglin, J., Seaberg, M. H., Zhao, Y., Bajt, S., Grant, T., Mariani, V., Nelson, G., Subramanian, G., Bae, E., Fromme, R., Fung, R., Schwander, P., Frank, M., White, T. A., Weierstall, U., Zatsepin, N., Spence, J., Fromme, P., Chapman, H. N., Pollack, L., Tremblay, L., Ourmazd, A., Phillips, G. N. & Schmidt, M. (2018). *BMC Biol.* **16**, 59.

Orville, A. M. (2020). *Curr. Opin. Struct. Biol.* **65**, 193–208.

Palmer, G., Kellert, M., Wang, J., Emons, M., Wegner, U., Kane, D., Pallas, F., Jezynski, T., Venkatesan, S., Rompotis, D., Brambrink, E., Monoszlai, B., Jiang, M., Meier, J., Kruse, K., Pergament, M. & Lederer, M. J. (2019). *J. Synchrotron Rad.* **26**, 328–332.

Pandey, S., Bean, R., Sato, T., Poudyal, I., Bielecki, J., Cruz Villarreal, J., Yefanov, O., Mariani, V., White, T. A., Kupitz, C., Hunter, M., Abdellatif, M. H., Bajt, S., Bondar, V., Echelmeier, A., Doppler, D., Emons, M., Frank, M., Fromme, R., Gevorkov, Y., Giovanetti, G.,

Jiang, M., Kim, D., Kim, Y., Kirkwood, H., Klimovskaia, A., Knoska, J., Koua, F. H. M., Letrun, R., Lisova, S., Maia, L., Mazalova, V., Meza, D., Michelat, T., Ourmazd, A., Palmer, G., Ramilli, M., Schubert, R., Schwander, P., Silenzi, A., Sztuk-Dambietz, J., Tolstikova, A., Chapman, H. N., Ros, A., Barty, A., Fromme, P., Mancuso, A. P. & Schmidt, M. (2020). *Nat. Methods*, **17**, 73–78.

Pandey, S., Calvey, G., Katz, A. M., Malla, T. N., Koua, F. H. M., Martin-Garcia, J. M., Poudyal, I., Yang, J.-H., Vakili, M., Yefanov, O., Zielinski, K. A., Bajt, S., Awel, S., Doerner, K., Frank, M., Gelisio, L., Jernigan, R., Kirkwood, H., Kloos, M., Koliyadu, J., Mariani, V., Miller, M. D., Mills, G., Nelson, G., Olmos, J. L., Sadri, A., Sato, T., Tolstikova, A., Xu, W., Ourmazd, A., Spence, J. H. C., Schwander, P., Barty, A., Chapman, H. N., Fromme, P., Mancuso, A. P., Phillips, G. N., Bean, R., Pollack, L. & Schmidt, M. (2021). *IUCrJ*, **8**, 878–895.

Roessler, C. G., Agarwal, R., Allaire, M., Alonso-Mori, R., Andi, B., Bachega, J. F. R., Bommer, M., Brewster, A. S., Browne, M. C., Chatterjee, R., Cho, E., Cohen, A. E., Cowan, M., Datwani, S., Davidson, V. L., Defever, J., Eaton, B., Ellson, R., Feng, Y. P., Ghislain, L. P., Glownia, J. M., Han, G. Y., Hattne, J., Hellmich, J., Héroux, A., Ibrahim, M., Kern, J., Kuczewski, A., Lemke, H. T., Liu, P. H., Majlof, L., McClintock, W. M., Myers, S., Nelsen, S., Olechno, J., Orville, A. M., Sauter, N. K., Soares, A. S., Soltis, S. M., Song, H., Stearns, R. G., Tran, R., Tsai, Y., Uervirojnangkoorn, M., Wilmot, C. M., Yachandra, V., Yano, J., Yukl, E. T., Zhu, D. L. & Zouni, A. (2016). *Structure*, **24**, 631–640.

Rowlinson, J. S. & Windom, B. (1982). *Molecular Theory of Capillarity*. Mineola: Dover Publication.

Schneider, C. A., Rasband, W. S. & Eliceiri, K. W. (2012). *Nat. Methods*, **9**, 671–675.

Schulz, J., Bielecki, J., Doak, R. B., Dörner, K., Graceffa, R., Shoeman, R. L., Sikorski, M., Thute, P., Westphal, D. & Mancuso, A. P. (2019). *J. Synchrotron Rad.* **26**, 339–345.

Sierra, R. G., Gati, C., Laksmono, H., Dao, E. H., Gul, S., Fuller, F., Kern, J., Chatterjee, R., Ibrahim, M., Brewster, A. S., Young, I. D., Michels-Clark, T., Aquila, A., Liang, M., Hunter, M. S., Koglin, J. E., Boutet, S., Junco, E. A., Hayes, B., Bogan, M. J., Hampton, C. Y., Puglisi, E. V., Sauter, N. K., Stan, C. A., Zouni, A., Yano, J., Yachandra, V. K., Soltis, S. M., Puglisi, J. D. & DeMirci, H. (2016). *Nat. Methods*, **13**, 59–62.

Sierra, R. G., Laksmono, H., Kern, J., Tran, R., Hattne, J., Alonso-Mori, R., Lassalle-Kaiser, B., Glöckner, C., Hellmich, J., Schafer, D. W., Echols, N., Gildea, R. J., Grosse-Kunstleve, R. W., Sellberg, J., McQueen, T. A., Fry, A. R., Messerschmidt, M. M., Miahnahri, A., Seibert, M. M., Hampton, C. Y., Starodub, D., Loh, N. D., Sokaras, D., Weng, T.-C., Zwart, P. H., Glatzel, P., Milathianaki, D., White, W. E., Adams, P. D., Williams, G. J., Boutet, S., Zouni, A., Messinger, J., Sauter, N. K., Bergmann, U., Yano, J., Yachandra, V. K. & Bogan, M. J. (2012). *Acta Cryst.* D**68**, 1584–1587.

Stagno, J. R., Liu, Y., Bhandari, Y. R., Conrad, C. E., Panja, S., Swain, M., Fan, L., Nelson, G., Li, C., Wendel, D. R., White, T. A., Coe, J. D., Wiedorn, M. O., Knoska, J., Oberthuer, D., Tuckey, R. A., Yu, P., Dyba, M., Tarasov, S. G., Weierstall, U., Grant, T. D., Schwieters, C. D., Zhang, J., Ferré-D'Amaré, A. R., Fromme, P., Draper, D. E., Liang, M., Hunter, M. S., Boutet, S., Tan, K., Zuo, X., Ji, X., Barty, A., Zatsepin, N. A., Chapman, H. N., Spence, J. C. H., Woodson, S. A. & Wang, Y. X. (2016). *Nature*, **541**, 242–246.

Stauch, B. & Cherezov, V. (2018). *Annu. Rev. Biophys.* **47**, 377–397.

Tenboer, J., Basu, S., Zatsepin, N., Pande, K., Milathianaki, D., Frank, M., Hunter, M., Boutet, S., Williams, G. J., Koglin, J. E., Oberthuer, D., Heymann, M., Kupitz, C., Conrad, C., Coe, J., Roy-Chowdhury, S., Weierstall, U., James, D., Wang, D., Grant, T., Barty, A., Yefanov, O., Scales, J., Gati, C., Seuring, C., Srajer, V., Henning, R., Schwander, P., Fromme, R., Ourmazd, A., Moffat, K., Van Thor, J. J., Spence, J. C. H., Fromme, P., Chapman, H. N. & Schmidt, M. (2014). *Science*, **346**, 1242–1246.

Tiab, D. & Donaldson, E. C. (2012). *Petrophysics*, pp. 371–418. Oxford: Gulf Professional Publishing.

Wang, D., Weierstall, U., Pollack, L. & Spence, J. (2014). *J. Synchrotron Rad.* **21**, 1364–1366.

Weierstall, U., James, D., Wang, C., White, T. A., Wang, D. J., Liu, W., Spence, J. C. H., Bruce Doak, R., Nelson, G., Fromme, P., Fromme, R., Grotjohann, I., Kupitz, C., Zatsepin, N. A., Liu, H. G., Basu, S., Wacker, D., Won Han, G., Katritch, V., Boutet, S., Messerschmidt, M., Williams, G. J., Koglin, J. E., Marvin Seibert, M., Klinker, M., Gati, C., Shoeman, R. L., Barty, A., Chapman, H. N., Kirian, R. A., Beyerlein, K. R., Stevens, R. C., Li, D. F., Shah, S. T. A., Howe, N., Caffrey, M. & Cherezov, V. (2014). *Nat. Commun.* **5**, 3309.

Wiedorn, M. O., Oberthür, D., Bean, R., Schubert, R., Werner, N., Abbey, B., Aepfelbacher, M., Adriano, L., Allahgholi, A., Al-Qudami, N., Andreasson, J., Aplin, S., Awel, S., Ayyer, K., Bajt, S., Barák, I., Bari, S., Bielecki, J., Botha, S., Boukhelef, D., Brehm, W., Brockhauser, S., Cheviakov, I., Coleman, M. A., Cruz-Mazo, F., Danilevski, C., Darmanin, C., Doak, R. B., Domaracky, M., Dörner, K., Du, Y., Fangohr, H., Fleckenstein, H., Frank, M., Fromme, P., Gañán-Calvo, A. M., Gevorkov, Y., Giewekemeyer, K., Ginn, H. M., Graafsma, H., Graceffa, R., Greiffenberg, D., Gumprecht, L., Göttlicher, P., Hajdu, J., Hauf, S., Heymann, M., Holmes, S., Horke, D. A., Hunter, M. S., Imlau, S., Kaukher, A., Kim, Y., Klyuev, A., Knoška, J., Kobe, B., Kuhn, M., Kupitz, C., Küpper, J., Lahey-Rudolph, J. M., Laurus, T., Le Cong, K., Letrun, R., Xavier, P. L., Maia, L., Maia, F., Mariani, V., Messerschmidt, M., Metz, M., Mezza, D., Michelat, T., Mills, G., Monteiro, D. C. F., Morgan, A., Mühlig, K., Munke, A., Münnich, A., Nette, J., Nugent, K. A., Nuguid, T., Orville, A. M., Pandey, S., Pena, G., Villanueva-Perez, P., Poehlsen, J., Previtali, G., Redecke, L., Riekehr, W. M., Rohde, H., Round, A., Safenreiter, T., Sarrou, I., Sato, T., Schmidt, M., Schmitt, B., Schönherr, R., Schulz, J., Sellberg, J. A., Seibert, M. M., Seuring, C., Shelby, M. L., Shoeman, R. L., Sikorski, M., Silenzi, A., Stan, C. A., Shi, X., Stern, S., Sztuk-Dambietz, J., Szuba, J., Tolstikova, A., Trebbin, M., Trunk, U., Vagovic, P., Ve, T., Weinhausen, B., White, T. A., Wrona, K., Xu, C., Yefanov, O., Zatsepin, N., Zhang, J., Perbandt, M., Mancuso, A. P., Betzel, C., Chapman, H. & Barty, A. (2018). *Nat. Commun.* **9**, 4025.

Zhang, H. T., Unal, H., Gati, C., Han, G. W., Liu, W., Zatsepin, N. A., James, D., Wang, D. J., Nelson, G., Weierstall, U., Sawaya, M. R., Xu, Q. P., Messerschmidt, M., Williams, G. J., Boutet, S., Yefanov, O. M., White, T. A., Wang, C., Ishchenko, A., Tirupula, K. C., Desnoyer, R., Coe, J., Conrad, C. E., Fromme, P., Stevens, R. C., Katritch, V., Karnik, S. S. & Cherezov, V. (2015). *Cell*, **161**, 833–844.